ARTICLES SCIENCE CHINA Materials

mater.scichina.com link.springer.com

Published online 13 February 2018 | https://doi.org/10.1007/s40843-018-9222-4

Sci China Mater 2018, 61(6): 822–830

SPECIAL ISSUE: Advanced Materials for Photoelectrochemical Cells

Engineering oxygen vacancy on rutile TiO_2 for efficient electron-hole separation and high solar-driven photocatalytic hydrogen evolution

Fang Xiao[1], Wei Zhou[2*], Bojing Sun[2], Haoze Li[2], Panzhe Qiao[2], Liping Ren[2], Xiaojun Zhao[1*] and Honggang Fu[2*]

ABSTRACT **Oxygen vacancy (V_O) plays a vital role in semiconductor photocatalysis. Rutile TiO_2 nanomaterials with controllable contents of V_O (0–2.18%) are fabricated *via* an *in-situ* solid-state chemical reduction strategy, with color from white to black. The bandgap of the resultant rutile TiO_2 is reduced from 3.0 to 2.56 eV, indicating the enhanced visible light absorption. The resultant rutile TiO_2 with optimal contents of V_O (~2.07%) exhibits a high solar-driven photocatalytic hydrogen production rate of 734 μmol h^{-1}, which is about four times as high as that of the pristine one (185 μmol h^{-1}). The presence of V_O elevates the apparent Fermi level of rutile TiO_2 and promotes the efficient electron-hole separation obviously, which favor the escape of photogenerated electrons and prolong the life-time (7.6×10^3 ns) of photogenerated charge carriers, confirmed by scanning Kelvin probe microscopy, surface photovoltage spectroscopy and transient-state fluorescence. V_O-mediated efficient photogenerated electron-hole separation strategy may provide new insight for fabricating other high-performance semiconductor oxide photocatalysts.**

Keywords: oxygen vacancy, rutile TiO_2, surface engineering, solar-driven photocatalysis, hydrogen evolution

INTRODUCTION

Hydrogen is considered as an environmental renewable energy source due to its high energy density and environment friendly [1]. Hence, photocatalytic hydrogen production attracts much more attention recently [2–4]. Since Fujishima and Honda [5–7] discovered hydrogen production from water splitting on TiO_2 for the first time, it is considered as the most promising photocatalyst candidate due to nontoxicity, high stability and low-cost [8–10]. Therefore, TiO_2 is widely used in photocatalytic degradation of pollutants, photocatalytic hydrogen production, solar cells, photoelectrochemical devices, and so on [11–14]. It is well-known that TiO_2 has three different crystal phases, anatase, brookite and rutile [15]. Notably, the rutile TiO_2 has attracted great research interest due to the fact that it is the most stable phase in thermodynamics, compared to the other two crystalline phases [16–18]. Rutile TiO_2 is suitable for photocatalytic water splitting due to its appropriate band energy position. The photocatalytic activity of rutile TiO_2 is usually low mainly due to the less surface active sites and the high recombination rate of photogenerated electron-hole pairs [19–21], although some researchers obtained rutile TiO_2 with excellent photocatalytic performance by designing and controlling suitable structure [19,20]. Moreover, rutile TiO_2 absorbs only ultraviolet light due to the wide bandgap (~3.0 eV), which represents a small fraction of solar energy and limits the efficiency of solar-driven photocatalysis greatly [22].

Recent studies have shown that surface defects could narrow the bandgap of TiO_2 and promote the separation of photogenerated charge carriers [23–25]. Moreover, since Mao *et al.* [26] reported a novel strategy to synthesize the high performance TiO_2 with surface defects by hydrogenation, more and more researchers are working on TiO_2 with surface defects [27–30]. Because the rutile

[1] Tianjin Key Laboratory of Structure and Performance for Functional Molecules, Key Laboratory of Inorganic–Organic Hybrid Functional Materials Chemistry (Tianjin Normal University), Ministry of Education of China; College of Chemistry, Tianjin Normal University, Tianjin 300387, China
[2] Key Laboratory of Functional Inorganic Material Chemistry, Ministry of Education of China, Heilongjiang University, Harbin 150080, China
* Corresponding authors (emails: zwchem@hotmail.com (W Zhou); Hxxyzhxj@mail.tjnu.edu.cn (X Zhao); fuhg@vip.sina.com (H Fu))

TiO_2 is extremely stable thermodynamically and has less surface defects than the anatase TiO_2, constructing rutile TiO_2 with surface defects is promising to have enhanced photocatalytic activity. Surface oxygen vacancy (V_O), as one of the most important surface defects of TiO_2, receives extensive attention [31–35]. Too low or high content of V_O defects are not conducive to narrowing the bandgap and improving the separation efficiency of photogenerated electron-hole pairs. The former could not offer adequate surface active sites and the latter will become the recombination centers of photogenerated charge carriers. Therefore, the effective control of V_O defects for rutile TiO_2 is still a challenge for further improving the solar-driven photocatalytic performance.

In this paper, we demonstrate a facile route to fabricate rutile TiO_2 nanomaterials with controllable contents of V_O (0–2.18%) defects *via* an *in-situ* solid-state chemical reduction strategy. The photoresponse of the rutile TiO_2 with narrow bandgap extends to visible light region. The obtained rutile TiO_2 with optimal contents of V_O (~2.07%) exhibits the highest solar-driven photocatalytic hydrogen production rate of 734 μmol h^{-1}, which is about four times as high as that of the pristine one (185 μmol h^{-1}). It is ascribed to the high separation efficiency and long life-time of photogenerated charge carriers in the presence of V_O. The photocatalytic mechanism of V_O-mediated efficient electron-hole separation for rutile TiO_2 is also proposed.

EXPERIMENTAL SECTION

Synthesis of rutile TiO_2 with different contents of oxygen vacancy

In a typical, 4 g of commercial rutile TiO_2 (denoted as i, 98.8%) was mixed with 1.5 g of $NaBH_4$ (98%, Aladdin Reagent Company). After thoroughly ground for 30 min, the mixture was heated from room temperature (RT) to 250, 300, and 350°C (denoted as ii, iii and iv) for 1 h under nitrogen atmosphere with a heating rate of 5°C min^{-1}, respectively. After naturally cooling to RT, the obtained product was dispersed into water with vigorous stirring for 30 min and then aged for 24 h. The powder was washed with ethanol and deionized water for several times to remove unreacted $NaBH_4$, and dried at 60°C overnight, and finally the rutile TiO_2 with different contents of oxygen vacancy were obtained. Deionized water was used for all experiments.

Characterization

The crystal structure of rutile TiO_2 was characterized using X-ray diffraction (XRD, Bruker D8 Advance) with Cu Kα (λ = 1.5406 Å) radiation. The morphologies of these samples were detected by scanning electron microscope (SEM, Hitachi S-4800) with a Philips XL-30-ESEM-FEG instrument operated at 20 kV. Transmission electron microscopy (TEM) and high-resolution TEM (HRTEM) measurements at an accelerating voltage of 200 kV were carried out on a JEM-2100 microscope. X-ray photoelectron spectroscopy (XPS, Kratos, ULTRA AXIS DLD) was carried out with monochrome Al Kα ($h\nu$ = 1,486.6 eV) radiation. All binding energies were calibrated by referencing to the C 1s peak at 284.6 eV. Diffuse reflectance spectroscopy (DRS) was conducted on a UV/vis spectrophotometer (Shimadzu UV-2550). The bandgaps were estimated by extrapolating a linear part of the plots to $(\alpha h\nu)^2 = 0$. Nitrogen adsorption-desorption isotherms at 77 K were collected on an AUTOSORB-1 (Quantachrome Instruments) nitrogen adsorption apparatus. The Brunauer-Emmett-Teller (BET) equation was used to calculate the specific surface area. Raman measurements were performed with a Jobin Yvon HR 800 micro-Raman spectrometer in the range of 100–1,000 cm^{-1} at 457.9 nm. Scanning Kelvin probe (SKP) test (SKP5050 system, Scotland) was executed to evaluate the work function at ambient atmosphere. The photoluminescence (PL) spectra were measured by a PE LS 55 spectrofluoro-photometer with excitation wavelength of 332 nm. Surface photovoltage spectroscopy (SPS) measurements were carried out with a homebuilt apparatus equipped with a lock-in amplifier (SR830) synchronized with a light chopper (SR540). The powders were sandwiched between two indium tin oxide (ITO)-coated glass electrodes, and monochromatic light was passed from a 500 W xenon lamp through a double prism monochromator (SBP300).

Photocatalytic hydrogen generation

Photocatalytic hydrogen generation was measured using an online photocatalytic hydrogen generation system (AuLight, Beijing, CEL-SPH2N) at ambient temperature (20°C). During the photocatalytic hydrogen evolution reaction, 100 mg photocatalysts loaded with 0.2 wt% Pt were dispersed into an aqueous solution containing 25 vol% of methanol. Before irradiation, the reactor and the whole gas circulating system were fully degassed to remove air using a vacuum pump for 30 min. Before the light reaction, the sample were dispersed with ultrasonic for 5–10 min. An AM 1.5 solar power system (solar simulator (Oriel, USA) equipped with an AM 1.5G filter (Oriel, USA)) was used as the light irradiation source. The

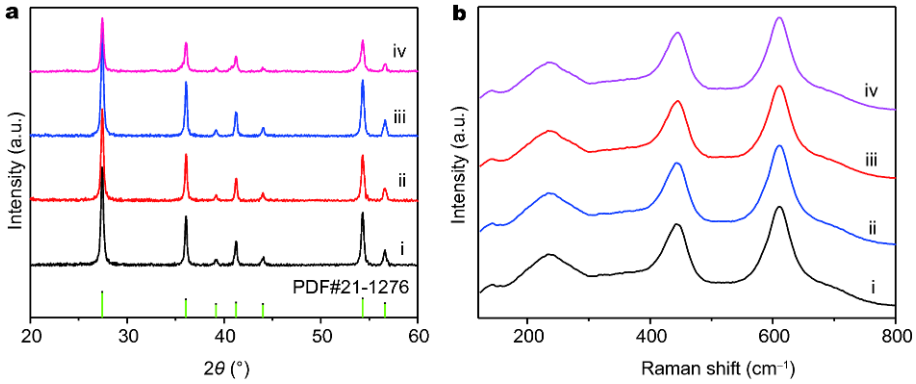

Figure 1 Typical XRD patterns (a) and Raman spectra (b) of pristine rutile TiO_2 (i) and hydrogenated rutile TiO_2 under 250°C (ii), 300°C (iii), and 350°C (iv), respectively.

photocatalytic H_2 evolution was analyzed using a gas chromatograph (SP7800, TCD, molecular sieves 5 Å, N_2 carrier, Beijing Keruida Limited). The apparent quantum efficiency for hydrogen generation was determined using the same system under illumination of a 300 W Xe lamp with a filter (365, 420 and 520 nm) system.

Photoelectrochemical properties

The photoelectrochemical properties of the samples were investigated using an electrochemical workstation (Princeton Versa STAT) with a platinum counter electrode and standard calomel reference electrode. The electrochemical properties were analyzed at RT. An aqueous solution of NaOH (1 mol L^{-1}) was used as the electrolyte. In detail, 0.1 g of the powder was dispersed into 3 mL ethanol under magnetic stirring, and then sprayed onto the 2 cm^2 ITO substrate at 70°C. The electrochemical impedance spectroscopic (EIS) measurements were carried out at 10 mV oscillation amplitude in the frequency range from 0.05 Hz to 10 kHz.

RESULTS AND DISCUSSION

XRD patterns were employed to analyze the crystal phase of the four TiO_2 samples (Fig. 1a). All samples exhibit typical diffraction peaks at around 2θ = 27.4°, 36.1°, 39.2°, 41.2°, 44.1°, 54.3° and 56.6°, corresponding to the (110), (101), (200), (111), (210), (211) and (220) planes of rutile TiO_2 (PDF#21-1276). In addition, with increasing calcination temperature, the diffraction peaks becomes weak and broad gradually, combined with the refined lattice parameter *c* from 2.959 to 2.958 Å, which may be attributed to the formation of surface oxygen vacancy decreasing the crystallinity of rutile TiO_2 and the distortion of the crystal structure [36]. Raman spectra of the four samples determined the crystalline structure of the samples, as shown in Fig. 1b. The peaks at 142, 446 and 610 cm^{-1} are correlated well with typical rutile Raman bands of B_{1g}, E_g and A_{1g}, respectively [37]. The peak at 239 cm^{-1} is attributed to the multi-proton scattering process [38]. Moreover, compared with sample i, the broadening of these peaks for sample ii-iv further demonstrates that surface oxygen vacancies break down the symmetry of rutile TiO_2 lattice after the *in-situ* solid-state chemical reduction process [39,40], consistent well with the XRD results.

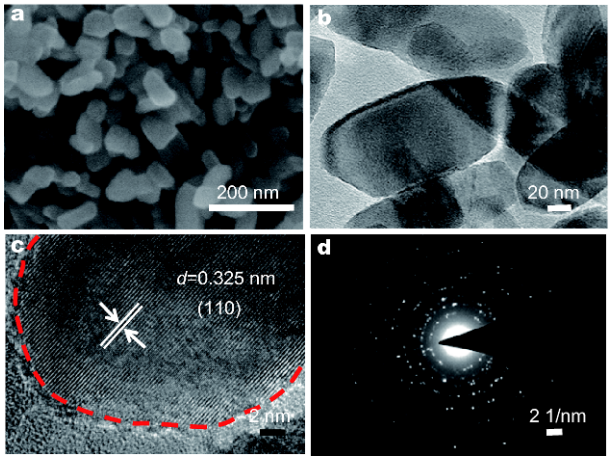

Figure 2 SEM (a), TEM (b), HRTEM images (c) and the corresponding selected-area electron diffraction pattern (d) of the hydrogenated rutile TiO_2 (300°C).

Fig. 2a–c show the SEM, TEM and HRTEM images of the hydrogenated rutile TiO_2 (sample iii), which has an average size of approximately 100 nm. The lattice spacing of 0.325 nm corresponds to the (110) plane of rutile TiO_2. Obviously, a disordered thin layer is formed on the sample surface after hydrogenation, which proved that the reduction reaction occurred on the surface of TiO_2.

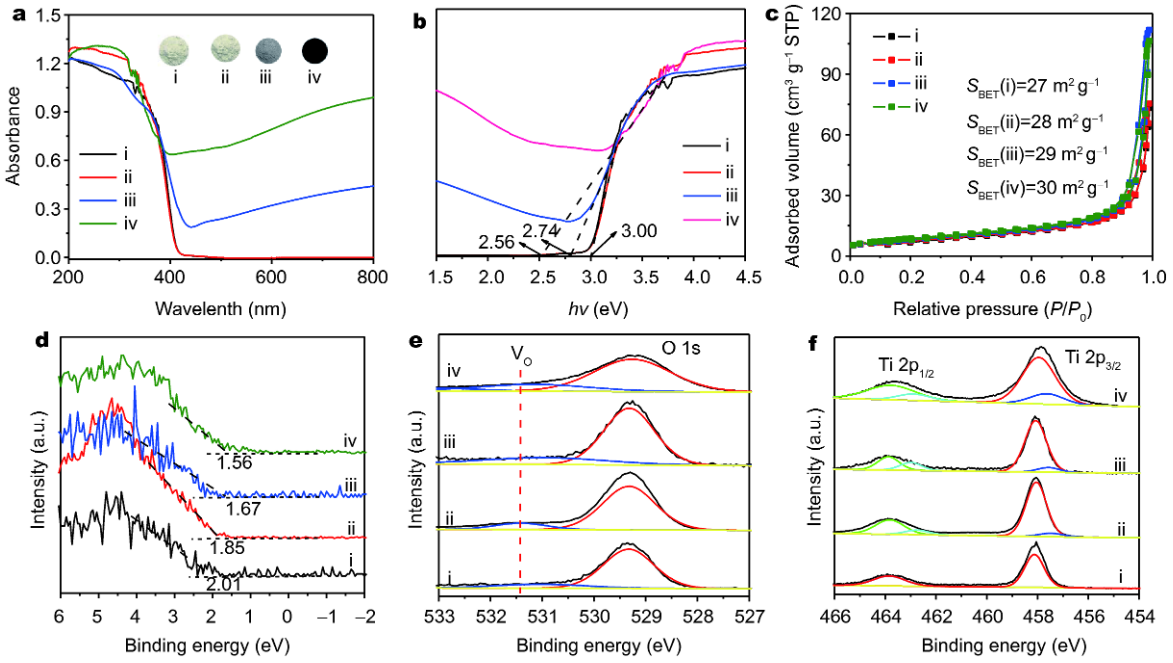

Figure 3 The UV/vis absorption spectra (a), the corresponding optical bandgaps (b), N_2 adsorption-desorption isotherms (c), XPS of valence band spectra (d), O 1s (e) and Ti 2p (f) of the pristine rutile TiO_2 (i) and the hydrogenated rutile TiO_2 under 250°C (ii), 300°C (iii), and 350°C (iv), respectively. The inset of (a) is the digital photos of sample i–iv.

The selected area electron diffraction (SAED) pattern (Fig. 2d) presents well-resolved diffraction rings and many diffraction spots, indicating the high crystallinity of phase-pure rutile. Compared to the pristine rutile TiO_2, the similar SAED pattern in Fig. S1 implies that the hydrogenated rutile TiO_2 remains the morphology and crystal bulk phase composition, although the surface phase is modified, which is consistent with the XRD and Raman results.

The UV/vis diffuse reflectance spectra are shown in Fig. 3a. A sharp increase in absorption at wavelengths shorter than 400 nm can be attributed to the inherent band gap absorption of crystalline rutile TiO_2. Obviously, the absorption edges extend to visible light region for sample ii-iv after reduction, with the color from white to black (the inset of Fig. 3a). The absorption in visible light region increases with increasing calcination temperature, due to the formation of surface oxygen vacancy. The surface disordered layers of the black rutile TiO_2 can form mid-gap states, which favor the visible light absorption [30]. The bandgap energies for sample i–iv are 3.0, 3.0, 2.74 and 2.56 eV, respectively (Fig. 3b), with the increase of calcining temperature, illustrating more surface oxygen vacancy. The narrowed bandgap is beneficial for visible light photocatalysis. Fig. 3c shows the N_2 adsorption-desorption isotherms of the four as-prepared samples are type IV according to the IUPAC classification and indicate the existence of mesopores within the interparticles [41]. The BET specific surface areas of the four samples are slightly changed, indicating no changed in the structure, as shown in the inset of Fig. 3c. Fig. 3d shows the typical XPS valence band (VB) characteristic curves of the four different rutile TiO_2 samples. The edge of the maximum energy for the pristine TiO_2 is about 2.01 eV, while the VB maximum energy for hydrogenated TiO_2 displays blue-shifts. The edges of the VB maximum energy for sample ii, iii and iv are about 1.85, 1.77 and 1.56 eV, respectively, which are lower than that of the pristine TiO_2, further indicating the efficient surface reduction. The elevation of VB for black rutile TiO_2 results in narrow bandgaps. In order to reveal the change of chemical bonds on the surface of rutile TiO_2, the XPS of Ti 2p and O 1s are shown in Fig. 3e and f, respectively. In Fig. 3e, the strong peak centered at 529.3 eV is assigned to lattice oxygen. The broader peak at 531.4 eV is attributed to the oxygen atoms in the vicinity of an oxygen vacancy (V_O) on TiO_2 surface after hydrogenation (Ti–OH) [42]. The percentage of V_O of sample i–iv is 0, 1.91%, 2.07% and 2.18%, respectively, calculated according to the peak area values of Ti^{3+} and Ti^{4+} [43].

For pristine rutile TiO_2, the main peaks of Ti^{4+} at 458.2 and 330.1 eV are attributed to Ti $2p_{1/2}$ and Ti $2p_{3/2}$. But

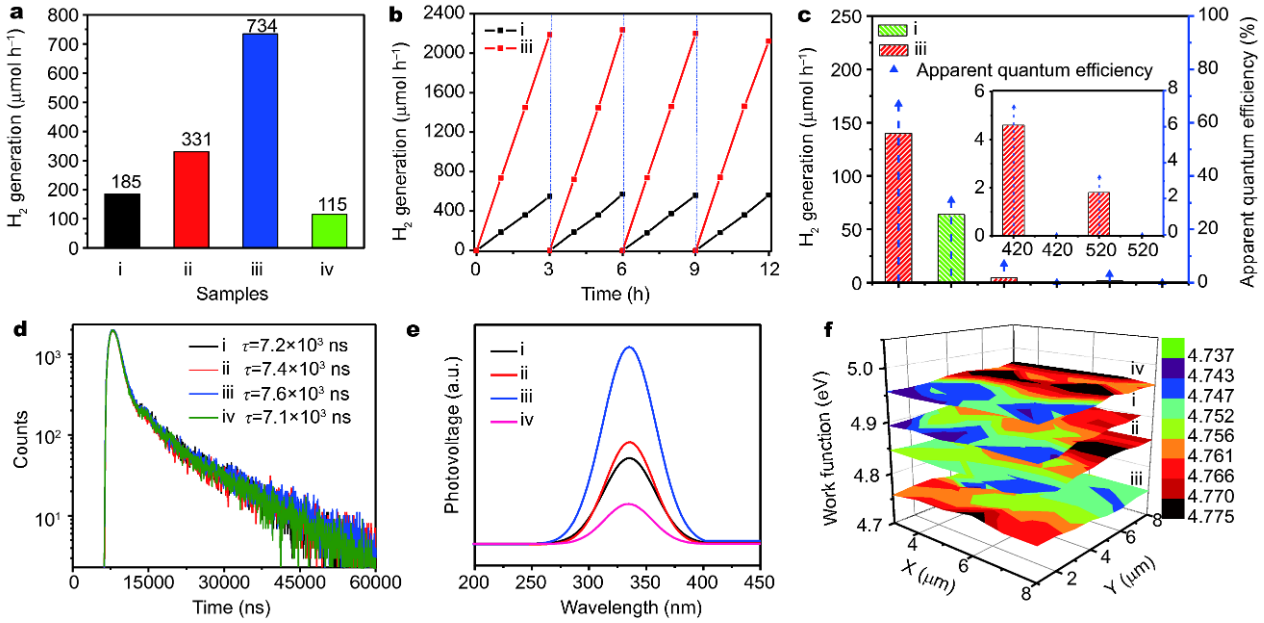

Figure 4 (a) Photocatalytic hydrogen evolution rates, (b) cycling tests of photocatalytic hydrogen generation under AM 1.5 irradiation, (c) the single-wavelength photocatalytic hydrogen evolution rates, (d) transient-state fluorescence spectrum, (e) surface photovoltage spectroscopy, (f) scanning Kelvin probe maps of pristine rutile TiO_2 (i) and hydrogenated rutile TiO_2 under 250°C (ii), 300°C (iii), and 350°C (iv), respectively. The inset of (c) enlarges the AQE of single-wavelength light at 420 and 520 nm.

after reduced by $NaBH_4$, the peaks of Ti^{3+} located at 457.6 and 463 eV are different from the pristine rutile TiO_2. The shift to lower binding energy of these peaks is attributed to the formation of Ti^{3+} on the surface disordered layer [44]. Additionally, no peak for $NaBH_4$ is observed (Fig. S2).

The photocatalytic activity is evaluated by photocatalytic hydrogen production under AM 1.5 irradiation. The hydrogen production of four samples is shown in Fig. 4a. Sample iii shows the highest photocatalytic activity with a reaction rate of 734 μmol h^{-1} that is about four times higher than that of the pristine TiO_2 (185 μmol h^{-1}) under AM 1.5 with a power density of 100 mW cm^{-2} based on 100 mg of the catalysts. In order to determine the stability of the photocatalytic activity, cycle tests within 12 h were carried out (the reactor was replenished with 5 mL solution with a volume ration equal to 1/4 of methanol/water before each cycling test). As shown in Fig. 4b, the H_2 production of sample iii remained nearly constant after four cycles (12 h), indicating high stability. After photocatalytic reaction, the crystalline structure nearly keeps intact (Fig. S3), further verifying its high stability. Moreover, the hydrogen production was also carried out under single wavelength light irradiation. The hydrogen generation rate of sample iii at 365 nm is 139 μmol h^{-1}, which is much higher than that at 420 nm (4.6 μmol h^{-1}), 520 nm (1.8 μmol h^{-1}) (Fig. 4c), and that of pristine rutile TiO_2 at each single wavelength. It indicates that UV light makes the main contribution to exciting electrons for water splitting. According to Equation (1) [45], the apparent quantum efficiency (AQE) for sample iii is calculated to be 67%, 7.1% and 3.2% at 365, 420 and 520 nm, respectively. The result illuminates that the rutile TiO_2 after hydrogenation exhibits visible light catalytic activity.

$$\mathrm{AQE} = \frac{2 \times (\text{evolved } H_2 \text{ molecules})}{\text{incident photons}} \times 100\%. \quad (1)$$

The solid transient-state fluorescence was tested to determine the lifetime of photogenerated charge carriers. The result exhibits that the lifetime of photogenerated charge carriers for sample iii is the longest one (7.6×10^3 ns), which proves that appropriate hydrogenation helps to improve the separation of photogenerated electron from VB to conduction band. Further, SPS was used to characterize the separation efficiency of the photogenerated electron-hole pairs. A strong SPS peak at 345 nm (Fig. 4e) is attributed to the electron transitions from the VB to the conduction band (band-to-band transitions, O 2p-Ti 3d) [46]. The SPS peak intensity for sample iii is stronger than that of others, illustrating the high-efficient separation of photogenerated electron-hole

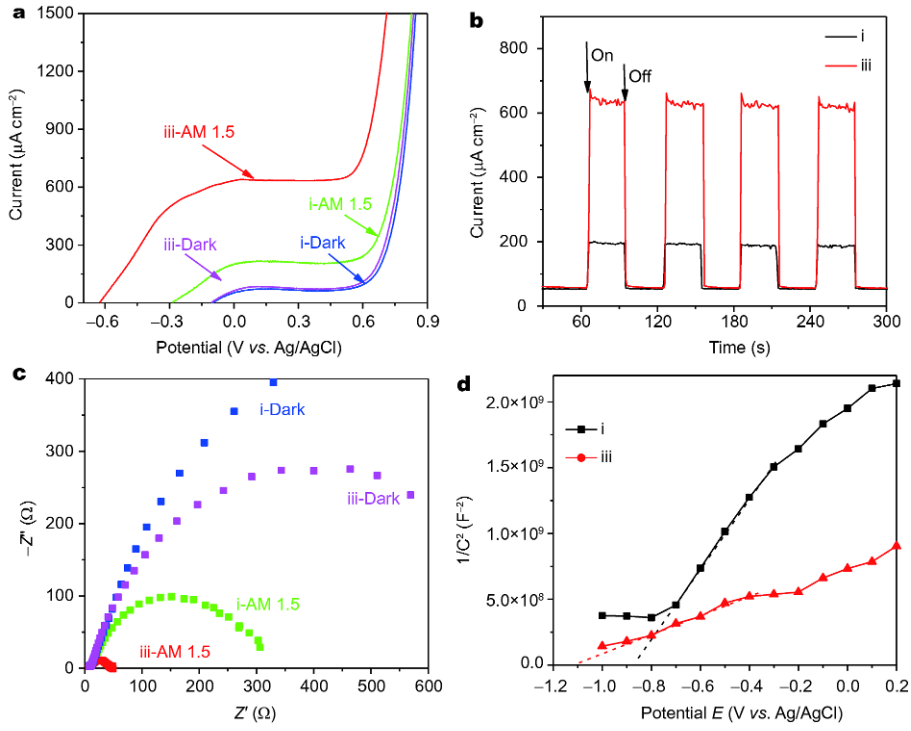

Figure 5 Photoelectrochemical properties of the pristine rutile TiO_2 (sample i) and the hydrogenated rutile TiO_2 (sample iii). (a) Linear sweeps voltammograms in the dark and under AM 1.5 irradiation, (b) the chronoamperometry, (c) the Nyquist plots of electrochemical impedance in the dark and under AM 1.5 irradiation, and (d) the Mott-Schottky plots.

pairs and long excitation life-times for the former [41]. Both the SPS and transient-state fluorescence results clearly suggest that sample iii is superior to other samples in photocatalytic hydrogen production, due to the high light harvesting, effective separation of photogenerated charge carriers and low recombination rate. As for sample iv, the life-time of photogenerated charge carriers decreases obviously, because superfluous surface V_O becomes the recombination centers of photogenerated electron-hole pairs. Scanning Kelvin probe microscopy (SKPM) was used to confirm the flat potential or Fermi level according to the work function [47]. The measured work functions of sample i–iv are 4.89, 4.84, 4.74 and 4.95 eV, respectively. The result illuminates that the Fermi level or flat band of sample iii is more negative than others. Simply, the valence electrons are much easier to be excited and transferred to the surface and rapidly captured by the adjacent co-catalysts, greatly restraining the electron-hole recombination and thus improving the photocatalytic performance.

Linear sweeps voltammogram of the pristine rutile TiO_2 and the hydrogenated rutile TiO_2 (sample iii, Fig. 5a) shows that the dark current density is almost constant within a broad applied bias range. The photocurrent density of sample iii under AM 1.5 is up to 635 μA cm^{-2}, which is much higher than that of the pristine one, indicating a more efficient charge separation. In Fig. 5b, the transient chronoamperometry of sample i and iii collected at 0.4 V displays prompt and constant on-off responses with light on-off. The current of sample iii (635 μA cm^{-2}) is approximately 3.6 times higher than that of sample i (173 μA cm^{-2}). Further, the photoelectronic responses for them at 0.4 V are almost constant, indicating their high stability. The smaller interfacial resistance of sample iii than that of sample i in EIS measurements, especially under AM 1.5 irradiation (Fig. 5c), indicates that sample iii has efficient charge mobility. The decrease of interface resistance is owing to the accumulation of photoelectrons at the interface and results in efficient charge separation, which is consistent with the SPS analysis. As shown in Fig. 5d, their Mott-Schottky plots have positive slope, suggesting that both materials are n-type semiconductors [48]. In addition, the sample iii shows a small slope compared with that of sample i, suggesting that the former has a higher donor density [49]. The richer donor density in sample iii could be ascribed to the V_O on the disordered layer, which is beneficial to improve the solar light photocatalytic activity.

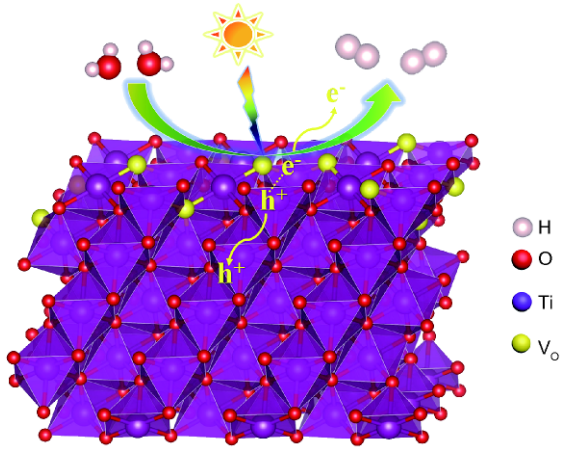

Figure 6 Schematic illustration of oxygen vacancy-mediated efficient photogenerated electron-hole separation in hydrogenated rutile TiO_2 photocatalytic hydrogen production.

The photocatalytic mechanism of V_O-mediated efficient photogenerated electron-hole separation in hydrogenated rutile TiO_2 is proposed in Fig. 6. In the presence of $NaBH_4$, the surface V_O defects and Ti^{3+} in disordered layers result in the narrowed bandgap. Then, the energy band positions of rutile TiO_2 are changed along with the degree of hydrogenation, as shown in Fig. S4. After reduction, the lift of CB for hydrogenated rutile TiO_2 promotes the separation efficiency of electron-hole pairs. The V_O favors the adsorption of water molecules and dissociation of hydrogen molecules, which plays vital role in exciting the water molecules and makes the generation and desorption of hydrogen molecules easily. Under solar light irradiation, the photogenerated electrons in the VB of hydrogenated rutile TiO_2 are excited to CB, and then transferred to the co-catalyst of Pt for proton reduction. The synergistic effect of Ti^{3+} and surface V_O defects is beneficial to the absorption of visible light, the rapid separation of photogenerated electron-hole pairs, and the inhibition of rapid recombination rate, thus enhancing solar-driven photocatalytic performance.

CONCLUSIONS

In summary, we demonstrated a facile sodium borohydride reduction method to prepare rutile TiO_2 photocatalyst with controllable V_O defects and high solar-driven photocatalytic activity. The experiments showed the formation of Ti^{3+} in the disordered layer and V_O defects on the surface of hydrogenated rutile TiO_2. The resulting hydrogenated rutile TiO_2 not only showed photoresponse extending to visible light region, but also increased the separation efficiency of photogenerated electron-hole pairs obviously. The hydrogenated rutile TiO_2 exhibited excellent solar-driven photocatalytic hydrogen evolution rate (734 μmol h^{-1}), which was almost four times as high as that of the pristine rutile TiO_2 (185 μmol h^{-1}), due to the V_O-mediated efficient electron-hole separation.

Received 2 January 2018; accepted 28 January 2018; published online 13 February 2018

1 Lin L, Zhou W, Gao R, *et al.* Low-temperature hydrogen production from water and methanol using Pt/α-MoC catalysts. Nature, 2017, 544: 80–83
2 Yuan YJ, Yu ZT, Chen DQ, *et al.* Metal-complex chromophores for solar hydrogen generation. Chem Soc Rev, 2017, 46: 603–631
3 Yang L, Li X, Zhang G, *et al.* Combining photocatalytic hydrogen generation and capsule storage in graphene based sandwich structures. Nat Commun, 2017, 8: 16049
4 Wang Q, Hisatomi T, Jia Q, *et al.* Scalable water splitting on particulate photocatalyst sheets with a solar-to-hydrogen energy conversion efficiency exceeding 1%. Nat Mater, 2016, 15: 611–615
5 Fujishima A, Honda K. Electrochemical photolysis of water at a semiconductor electrode. Nature, 1972, 238: 37–38
6 Fang WH, Zhang L, Zhang J. A 3.6 nm Ti_{52}–oxo nanocluster with precise atomic structure. J Am Chem Soc, 2016, 138: 7480–7483
7 Elbanna O, Fujitsuka M, Majima T. g-C_3N_4/TiO_2 mesocrystals composite for H_2 evolution under visible-light irradiation and its charge carrier dynamics. ACS Appl Mater Interfaces, 2017, 9: 34844–34854
8 Hussain H, Tocci G, Woolcot T, *et al.* Structure of a model TiO_2 photocatalytic interface. Nat Mater, 2017, 16: 461–466
9 Ren XN, Hu ZY, Jin J, *et al.* Cocatalyzing Pt/PtO phase-junction nanodots on hierarchically porous TiO_2 for highly enhanced photocatalytic hydrogen production. ACS Appl Mater Interfaces, 2017, 9: 29687–29698
10 Selcuk S, Selloni A. Facet-dependent trapping and dynamics of excess electrons at anatase TiO_2 surfaces and aqueous interfaces. Nat Mater, 2016, 15: 1107–1112
11 Sun Z, Liao T, Kou L. Strategies for designing metal oxide nanostructures. Sci China Mater, 2017, 60: 1–24
12 Niu M, Zhang J, Cao D. I, N-codoping modification of TiO_2 for enhanced photoelectrochemical H_2O splitting in visible-light region. J Phys Chem C, 2017, 121: 26202–26208
13 Qian L, Yu P, Zeng J, *et al.* Large-scale functionalization of biomedical porous titanium scaffolds surface with TiO_2 nanostructures. Sci China Mater, 2018, 61: 557–564
14 Guo L, Fei C, Zhang R, *et al.* Impact of sol aging on TiO_2 compact layer and photovoltaic performance of perovskite solar cell. Sci China Mater, 2016, 59: 710–718
15 Li R, Weng Y, Zhou X, *et al.* Achieving overall water splitting using titanium dioxide-based photocatalysts of different phases. Energy Environ Sci, 2015, 8: 2377–2382
16 Yu XY, Wu HB, Yu L, *et al.* Rutile TiO_2 submicroboxes with superior lithium storage properties. Angew Chem Int Ed, 2015, 54: 4001–4004
17 Wu T, Kang X, Kadi MW, *et al.* Enhanced photocatalytic hydrogen generation of mesoporous rutile TiO_2 single crystal with wholly exposed {111} facets. Chin J Catal, 2015, 36: 2103–2108
18 Maeda K, Ishimaki K, Okazaki M, *et al.* Cobalt oxide nanoclusters

on rutile titania as bifunctional units for water oxidation catalysis and visible light absorption: understanding the structure–activity relationship. ACS Appl Mater Interfaces, 2017, 9: 6114–6122
19 Nguyen-Phan TD, Luo S, Vovchok D, *et al.* Visible light-driven H_2 production over highly dispersed ruthenia on rutile TiO_2 nanorods. ACS Catal, 2016, 6: 407–417
20 Li L, Yan J, Wang T, *et al.* Sub-10 nm rutile titanium dioxide nanoparticles for efficient visible-light-driven photocatalytic hydrogen production. Nat Commun, 2015, 6: 5881
21 Kim W, Tachikawa T, Moon G, *et al.* Molecular-level understanding of the photocatalytic activity difference between anatase and rutile nanoparticles. Angew Chem Int Ed, 2014, 53: 14036–14041
22 Lun Pang C, Lindsay R, Thornton G. Chemical reactions on rutile TiO_2 (110). Chem Soc Rev, 2008, 37: 2328–2353
23 Yang Y, Liu G, Irvine JTS, *et al.* Enhanced photocatalytic H_2 production in core-shell engineered rutile TiO_2. Adv Mater, 2016, 28: 5850–5856
24 Zhao Z, Zhang X, Zhang G, *et al.* Effect of defects on photocatalytic activity of rutile TiO_2 nanorods. Nano Res, 2015, 8: 4061–4071
25 Schaub R, Thostrup P, Lopez N, *et al.* Oxygen vacancies as active sites for water dissociation on rutile TiO_2 (110). Phys Rev Lett, 2001, 87: 266104
26 Chen X, Liu L, Yu PY, *et al.* Increasing solar absorption for photocatalysis with black hydrogenated titanium dioxide nanocrystals. Science, 2011, 331: 746–750
27 Zhou W, Li W, Wang JQ, *et al.* Ordered mesoporous black TiO_2 as highly efficient hydrogen evolution photocatalyst. J Am Chem Soc, 2014, 136: 9280–9283
28 Tan H, Zhao Z, Niu M, *et al.* A facile and versatile method for preparation of colored TiO_2 with enhanced solar-driven photocatalytic activity. Nanoscale, 2014, 6: 10216–10223
29 Hu W, Zhou W, Zhang K, *et al.* Facile strategy for controllable synthesis of stable mesoporous black TiO_2 hollow spheres with efficient solar-driven photocatalytic hydrogen evolution. J Mater Chem A, 2016, 4: 7495–7502
30 Chen X, Liu L, Huang F. Black titanium dioxide (TiO_2) nanomaterials. Chem Soc Rev, 2015, 44: 1861–1885
31 Cushing SK, Meng F, Zhang J, *et al.* Effects of defects on photocatalytic activity of hydrogen-treated titanium oxide nanobelts. ACS Catal, 2017, 7: 1742–1748
32 Henkel B, Neubert T, Zabel S, *et al.* Photocatalytic properties of titania thin films prepared by sputtering versus evaporation and aging of induced oxygen vacancy defects. Appl Catal B-Environ, 2016, 180: 362–371
33 Weng X, Zeng Q, Zhang Y, *et al.* Facile approach for the syntheses of ultrafine TiO_2 nanocrystallites with defects and C heterojunction for photocatalytic water splitting. ACS Sustain Chem Eng, 2016, 4: 4314–4320
34 Zhang Y, Ding Z, Foster CW, *et al.* Oxygen vacancies evoked blue TiO_2(B) nanobelts with efficiency enhancement in sodium storage behaviors. Adv Funct Mater, 2017, 27: 1700856
35 Song H, Li C, Lou Z, *et al.* Effective formation of oxygen vacancies in black TiO_2 nanostructures with efficient solar-driven water splitting. ACS Sustain Chem Eng, 2017, 5: 8982–8987
36 Vásquez GC, Karazhanov SZ, Maestre D, *et al.* Oxygen vacancy related distortions in rutile TiO_2 nanoparticles: A combined experimental and theoretical study. Phys Rev B, 2016, 94: 235209
37 Zhang Y, Harris CX, Wallenmeyer P, *et al.* Asymmetric lattice vibrational characteristics of rutile TiO_2 as revealed by laser power dependent raman spectroscopy. J Phys Chem C, 2013, 117: 24015–24022
38 Vásquez GC, Maestre D, Cremades A, *et al.* Assessment of the Cr doping and size effects on the Raman-active modes of rutile TiO_2 by UV/visible polarized Raman spectroscopy. J Raman Spectrosc, 2017, 48: 847–854
39 Wu Y, Jiang Y, Shi J, *et al.* Multichannel porous TiO_2 hollow nanofibers with rich oxygen vacancies and high grain boundary density enabling superior sodium storage performance. Small, 2017, 13: 1700129
40 Naldoni A, Allieta M, Santangelo S, *et al.* Effect of nature and location of defects on bandgap narrowing in black TiO_2 nanoparticles. J Am Chem Soc, 2012, 134: 7600–7603
41 Zhou W, Sun F, Pan K, *et al.* Well-ordered large-pore mesoporous anatase TiO_2 with remarkably high thermal stability and improved crystallinity: preparation, characterization, and photocatalytic performance. Adv Funct Mater, 2011, 21: 1922–1930
42 Gao S, Sun Z, Liu W, *et al.* Atomic layer confined vacancies for atomic-level insights into carbon dioxide electroreduction. Nat Commun, 2017, 8: 14503
43 Liao X, Zhang Y, Hill M, *et al.* Highly efficient Ni/CeO_2 catalyst for the liquid phase hydrogenation of maleic anhydride. Appl Catal A-General, 2014, 488: 256–264
44 Tan S, Xing Z, Zhang J, *et al.* Ti^{3+}-TiO_2/g-C_3N_4 mesostructured nanosheets heterojunctions as efficient visible-light-driven photocatalysts. J Catal, 2018, 357: 90–99
45 Liu J, Liu Y, Liu N, *et al.* Metal-free efficient photocatalyst for stable visible water splitting *via* a two-electron pathway. Science, 2015, 347: 970–974
46 Kronik L, Shapira Y. Surface photovoltage phenomena: theory, experiment, and applications. Surf Sci Rep, 1999, 37: 1–206
47 Hu Y, Pecunia V, Jiang L, *et al.* Scanning Kelvin probe microscopy investigation of the role of minority carriers on the switching characteristics of organic field-effect transistors. Adv Mater, 2016, 28: 4713–4719
48 Zhang H, Wang G, Chen D, *et al.* Tuning photoelectrochemical performances of Ag–TiO_2 nanocomposites *via* reduction/oxidation of Ag. Chem Mater, 2008, 20: 6543–6549
49 Mao C, Zuo F, Hou Y, *et al. In situ* preparation of a Ti^{3+} self-doped TiO_2 film with enhanced activity as photoanode by N_2H_4 reduction. Angew Chem Int Ed, 2014, 53: 10485–10489

Acknowledgements This work was supported by the Key Program Projects of the National Natural Science Foundation of China (21631004) and the National Natural Science Foundation of China (51672073).

Author contributions Xiao F conducted the experiments; Zhou W, Zhao X and Fu H designed and engineered the work; Sun B, Li H, Qiao P and Ren L performed the characterization; Xiao F wrote the paper with support from Zhou W, Zhao X and Fu H. All authors contributed to the general discussion.

Conflict of interest These authors declared no conflict of interest.

Supplementary information Supplementary data are available in the online version of the paper.

Fang Xiao received her BSc degree in 2015 from Datong University, China. Her research interests are focused on rutile TiO_2 nanomaterials for photocatalysis.

Wei Zhou received his PhD degree in 2009 from Jilin University, China. Afterwards, he joined Prof. Honggang Fu's group at Heilongjiang University, and became a full professor in 2015. His research interests include mesoporous materials, semiconductor nanomaterials for solar energy conversion, photocatalysis, and their photothermal and photoelectrochemical performance.

Xiaojun Zhao received his BSc degree in 1982 from Tianjin Normal University, China. He received his MSc degree in 2001 and PhD degree in 2004 from Nankai University, China. Currently, he is a full professor at Tianjin Normal University. His research interests focus on inorganic-organic hybrid functional material.

Honggang Fu received his BSc degree in 1984 and MSc degree in 1987 from Jilin University, China. Then, he joined Heilongjiang University as an assistant professor. In 1999, he received his PhD degree from Harbin Institute of Technology, China. He became a full professor in 2000. Currently, he is also Cheung Kong Scholar Professor. His interests focus on oxide-based semiconductor nanomaterials for solar energy conversion and photocatalysis, and crystalline carbon-based nanomaterials for energy conversion and storage.

具有高效电子-空穴分离和优异太阳光催化产氢性能的金红石TiO_2表面的氧空位调控

肖芳[1], 周卫[2*], 孙博婧[2], 李昊泽[2], 乔盼哲[2], 任丽萍[2], 赵小军[1*], 付宏刚[2*]

摘要 氧空位缺陷在半导体光催化中起重要作用. 本文采用原位固态化学还原策略可控制备了具有不同氧空位含量(0~2.18%)的金红石TiO_2纳米材料, 其带隙由3.0 eV减小到2.56 eV, 颜色由白色变为黑色. 氧空位含量为~2.07%的样品具有最高的太阳光催化产氢性能(734 μmol h^{-1}), 产氢量约为原始样品(185 μmol h^{-1})的四倍. 扫描开尔文探针、表面光电压和瞬态荧光结果表明: 氧空位的出现提升了金红石TiO_2的表观费米能级并促进了光生电子-空穴的分离, 有利于光生电子的溢出和光生载流子寿命的延长(7.6×10^3 ns). 这种由氧空位缺陷诱导的光生电子-空穴高效分离策略为构筑其他高性能半导体氧化物光催化剂提供了新思路.

